Title

Effect of Structural Heterogeneity on Mechanical Deformation Behaviors of Metallic Materials

Permalink

https://escholarship.org/uc/item/27b200m4

Author

Wang, Han

Publication Date

2022

Peer reviewed|Thesis/dissertation

UNIVERSITY OF CALIFORNIA,
IRVINE

Effect of Structural Heterogeneity on Mechanical Deformation Behaviors of Metallic
Materials

THESIS

submitted in partial satisfaction of the requirements
for the degree of

MASTER OF SCIENCE

in Mechanical Engineering

by

Han Wang

Thesis Committee:
Assistant Professor Penghui Cao, Chair
Associate Professor Jaeho Lee
Associate Professor Yoonjin Won

2022

DEDICATION

To

my family and friends

in recognition of their worth to me

TABLE OF CONTENTS

LIST OF FIGURES

ACKNOWLEDGEMENTS

ABSTRACT OF THE THESIS

Effect of Structural Heterogeneity on Mechanical Deformation Behaviors of Metallic
Materials

by

Han Wang

Master of Science in Mechanical Engineering

University of California, Irvine, 2022

Assistant Professor Penghui Cao, Chair

A mixture of structural heterogeneity has been a promising way to design materials with excellent mechanical properties. Yet, the significance of how structural heterogeneity tunes the deformability and its associated deformation mechanisms is still not lucid. In this work, we dive into two types of metallic materials, namely nanotwinned metals and monoatomic Ta metallic glass, to address this issue. In nanotwinned metals, we survey a range of nanotwinned materials that possess different stacking fault energies (SFEs), and understand the TB strengthening limit. Distinct from Cu and Al, the nanotwinned, ultralow SEF materials (Co, NiCoCr, and NiCoCrFeMn) intriguingly exhibit a continuous strengthening down to a twin thickness of 0.63 nm. Examining dislocation slip mode and deformation microstructure, we find the hard dislocation modes persist even when reducing the twin boundary spacing to a nanometer regime. Meanwhile, the soft dislocation mode, which causes detwinning in Cu and Al, results in phase transformation and lamellar structure formation in Co, NiCoCr, and NiCoCrFeMn. In monoatomic Ta metallic glass, it is found that deformability is directly associated with inherent structural heterogeneity on the level of atomic order. We find the dispersive and sparse distribution of local order is associated with

necking, yet percolation of medium-range order constrains the deformability and results in brittle failure. These findings shed new light on the role of structural heterogeneity in metallic materials, which has important implications for the design of nanoscale metallic materials with tunable mechanical properties.

INTRODUCTION

Date back to ancient times, the wisdom of people has already employed the concept of structural heterogeneity in many shapes and forms of constructions and applications. Combined with soil and stones, the ancient people managed to build houses that were way stronger than that of pure soil. A mixture of heterogeneity allows the materials to acquire the merits of the good from each component. Yet, modern technologies have guaranteed the engineering of materials on the micro- or even nano-scales, opening a new era of designing materials with improved mechanical properties. As a result, understanding the role of structural heterogeneity becomes critical in making excellent materials for various applications.

Metallic materials, the most popular in the manufacturing industry, have also evolved progressively. Traditional polycrystalline metals generally suffer from a trade-off between strength and ductility[1], meaning increasing the strength is often coupled with compromised ductility. However, recently, a new rising class of heterogeneously structured polycrystalline metals, such as nanotwinned metals[2] and metals with gradient[3], bimodal[4], and lamellar[5] grain size distributions, tend to push forward the boundary of mechanical properties of traditional polycrystalline metals and achieve high ductility and strength at the same time. This means the structural heterogeneity intentionally engineered into the materials also triggers deformation mechanisms dissimilar to the traditional polycrystalline metals. On the other hand, metallic glasses, also known as amorphous metals, possess ultra-high strength but are also highly brittle[6,7]. Its amorphous nature makes it challenging to manipulate and understand the atomic structures and corresponding mechanical properties. Interestingly,

recent findings have shown that the features of MGs are closely associated with their fabrication and processing histories, and by either tuning processing history[8–10], a reduction of sample size[11], or even irradiation[12], it can increase the ductility to some extent. Yet, it does not alter the fact that metallic glasses are still amorphous, so what these methods are changing in the materials systems is still largely elusive.

In this work, we discuss how tuning structural heterogeneities affects the mechanical deformation mechanisms of metallic materials. We found that while decreasing the twin boundary spacing, the same nanotwinned polycrystalline structure can typically have two types of mechanical responses in varying stack fault energy (SFE) contexts, e.g., strengthening followed by softening or continuous strengthening without softening breakdown. By studying the individual grain-level mechanical deformation mechanisms, we found that the dislocation slip (soft mode) results in TB migration and annihilation in nanotwinned Al, originating from its high SFE and inclination to remove TB and SF. However, for materials with low SFE, the soft dislocation mode gives rise to hcp lamella formation and growth. More importantly, the hard dislocation modes, which occur at large twin boundary spacing, also prevail in reduced spacing (even at 0.63 nm). The consistency of the dislocation mechanisms and its insensitivity to twin thickness are manifested as continued strengthening in nanotwinned NiCoCr. Meanwhile, we use a similar method to understand the mechanical behavior transition from brittle fracture to ductile fracture by deforming monoatomic Ta metallic glass nanowires prepared from two thermal treatments (aged and rejuvenated). During straining, the atomic structure evolution has demonstrated that the structural heterogeneity, including short-range order and medium-range order, is essentially responsive to mechanical deformation, and the brittle to ductile transition is

2

more associated with the structural features of medium-range order rather than short-range order.

Chapter 1 Background

1.1 Nanotwinned metals

Nanotwinned polycrystalline metals can achieve ultrahigh strength without significantly losing ductility[13,14,15]. It contains twin boundaries (TBs) that alter the conventional crystalline packing orders so that it exhibits mirrored packing order beside one twin boundary (Figure 1.1a), which significantly influences the dislocation activities inside the grains. Based on the slip direction and slip plane, as shown by Figure 1.1b, there are typically three dislocation gliding modes: (1) slip transfer mode (STM), both slip direction and slip plane are inclined to the TB, (2) confined layer mode (CLM), slip direction is parallel to, but slip plane is inclined to the TB, (3) Parallel to TB slip mode (PTBM), both slip direction and slip plane are parallel to the TB. The exceptional mechanical performance associated with nanotwinned metals is attributed to the dislocation-TB interactions[16,17]. When varying the twin boundary spacing (twin thickness) from micro- to nanometer scale, nanotwinned metals first experience strengthening until reaching a small critical spacing. Further reducing the spacing leads to the softening-dominated regime. This strengthening-to-softening transition, occurring at nanometers depending on grain size[18], is governed by dislocation mechanism crossover from Hall-Petch type of strengthening (hard dislocation mode) to partial dislocation slip parallel to twin boundary (soft mode)[2]. This type of partial dislocation motion may result in TB migration and annihilation, or hexagonal close-packed lamellar formation (see schematic illustration in Figure 2.3), presumably hinged on the stacking fault energy (SFE)[19].

Besides pure metals with various positive SFEs, another emergent group of materials, multi-principal element alloys (MPEAs), often termed high-entropy alloys, enable tunable

SFE through tailoring composition[20] and chemical short-range order[21]. Intriguingly, some MPEA is hypothesized to possess an intrinsic negative SFE, suggested by the predominant stacking faulting mechanism during mechanical deformation[22]. This large SFE turnability motivates us to rethink the strengthening and softening effects in nanotwinned materials. Especially when the SFE turns into a low or even negative value, the question remains about how the corresponding dislocation mechanisms in nanotwinned systems are influenced. In this work, we consider five different materials, including Al, Cu, Co, NiCoCr, and NiCoCrFeMn, which cover a considerable variation of SFE (Figure 2.1c).

By performing atomistic simulation of uniaxial stretching deformation, we find the nanotwinned materials with high SFE exhibit softening regimes at a small twin boundary spacing λ; however, the low SFE materials show a continuous strengthening even with $\lambda < 1$ nm. By carefully examining the dislocation slip mode, deformation microstructure, and local strain map, it is found that, at small λ, the hard dislocation slip modes (slip transfer and confined layer slip) still persist, and the soft mode (dislocation slip parallel to TB) gives rise to hexagonal close-packed (hcp) phase formation and growth (martensite transformation).
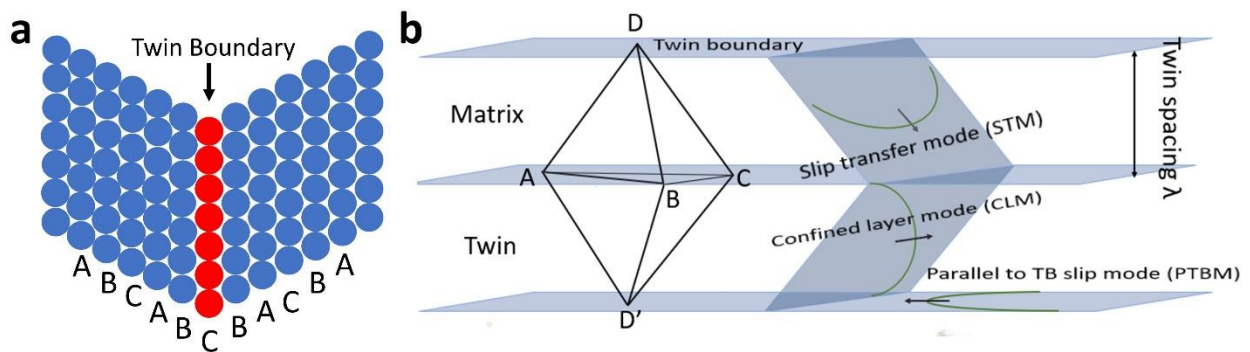

Figure 1.1 | Atomic structure and dislocation slip modes in nanotwinned metals. (a) TB in FCC crystals. (b) Three dislocation slip modes represented by a double Tompson tetrahedron.

5

2.2 Metallic glasses (MGs)

Unlike crystalline structures with ordered atomic packing patterns, MGs are amorphous with a liquid-like atomic arrangement. They possess unique mechanical properties, including ultra-high strength and excellent elasticity[7]. However, MGs generally suffer from poor ductility due to highly-localized inhomogeneous deformation from the formation and propagation of a few dominant shear bands[6,7]. Significant efforts have been made to enhance the deformability and, thus ductility of MGs by varying thermomechanical processing[8]. For a given MG, specific variations in their processing history[9,10], a reduction in sample size[11,23,24], and even irradiation[12] can facilitate, to some extent, homogeneous plastic flow to induce a brittle-to-ductile transition. Such a transition in deformation mode has often been ascribed to the so-called "rejuvenation" of MGs[8], although its microstructural origin remains largely elusive.

In classical theory[8], such history-dependent behavior of MGs has mainly been ascribed to the formation of different metastable states with distinct atomic packing and, thus mechanical responses. Rejuvenation was believed to reduce the atomic packing density and increase the free volume of MGs[25–27], thereby facilitating the formation of shear transformation zones (STZs) and enhancing the ductility[28]. However, previous studies merely presented the statistically-averaged volume information in bulk MGs via diffraction peak analyses[25–27], which cannot represent the intrinsic difference between atomic configurations or their evolution. At the atomic scale, MGs are composed of numerous structural heterogeneities, including short-range order (SRO) and medium-range order (MRO)[29,30]. Their spatial distributions and dynamic evolution should directly correlate with the deformability of MGs, which have yet to be elucidated. The impact of structural

heterogeneities, particularly the differences in SROs and MROs and their dynamic evolution, on the deformability and brittle-to-ductile transition of MGs remains an open question.

In this work, we uncover the microstructural origin of the brittle-to-ductile transition of monoatomic tantalum (Ta) MGs nanowires using massively parallel atomistic simulation. Monatomic MGs can largely eliminate the interference from chemical heterogeneity on the configuration of atomic clusters[25] and thus their effects on deformation dynamics. By tuning the thermal treatment history (aging and rejuvenation), we are able to tailor the microstructure motifs of MGs to induce different fracture modes (shear band or necking). By tracking the dynamic development of atomic microstructure features during straining, we reveal the significant roles of structural heterogeneity in controlling the brittle-to-ductile transition in monatomic Ta MGs. It is found that the brittle fracture mode is closely associated with a high order of structural heterogeneity in the initial structure, and the deformation tends to progressively destroy the preexisting order and leads to localized shear band fracture. However, the low order of structural heterogeneity in the rejuvenated Ta MG triggers a relaxation process and creates orders during straining, leading to a homogenous deformation flow, thus, ductile fracture mode.

Chapter 2 Strengthening and Softening in Nanotwinned Metals

In this chapter, we discuss in detail the mechanical deformation mechanisms associated with strengthening and softening in nanotwinned metals.
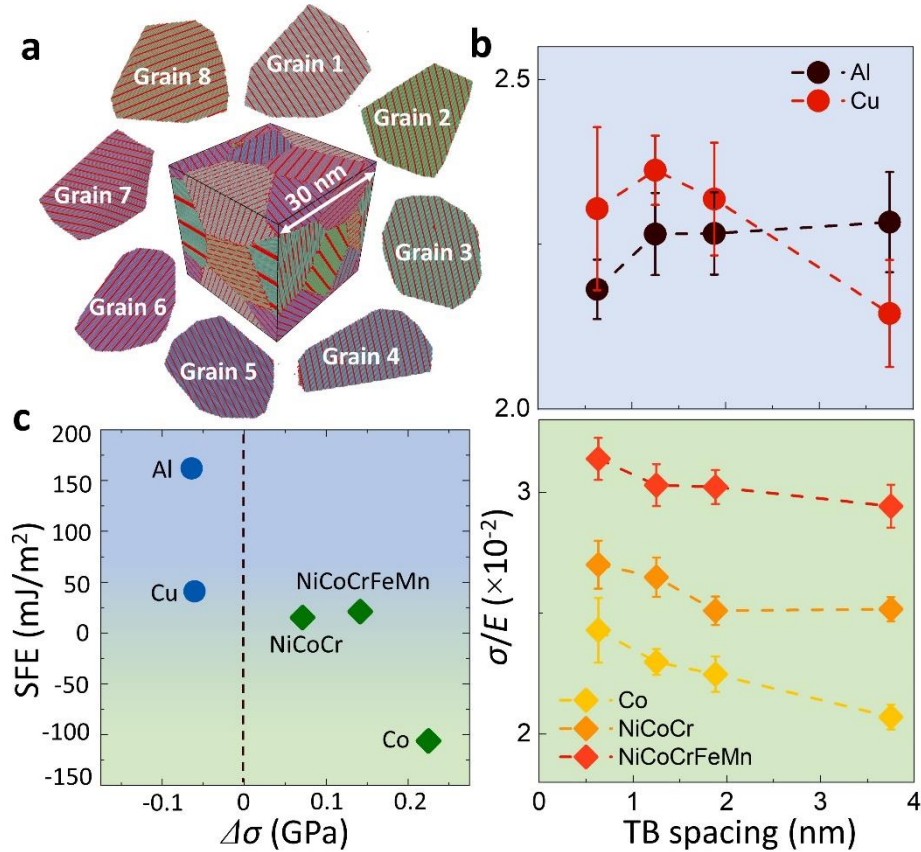
Figure 2.1 | The mechanical behavior of nanotwinned metals. (a) Polycrystalline and nanotwinned structures. The red-colored atoms indicate the twin boundary. **(b)** The plastic flow stress as a function of twin boundary spacing for Al and Cu (top panel), and Co, NiCoCr and NiCoCrFeMn (bottom). **(c)** The correlation between SFE and twin thickness-dependent stress change. The negative value of Δσ indicates softening, and the positive represents strengthening.

2.1 Simulation model and method

We consider polycrystalline-nanotwinned structures with dimensions of ~ 30 nm × 30 nm × 30 nm, consisting of 8 randomly orientated grains. By changing the twin boundary spacing λ, we generate a series of nanotwinned structures with λ varying from ~3.75 nm to ~0.63 nm. Figure 2.1a shows the polycrystalline structure (λ = 1.25 nm) and the 8

8

constituent grains. Keeping the same grain size and orientation, we generate the polycrystal

models for Al, Cu, Co, NiCoCr, and NiCoCrFeMn. The interatomic interactions are described

by embedded-atom method potentials[31,32,33,34, 35]. It is noted that the Co serves as a

surrogate model of negative SFE. Before straining, all structures are equilibrated at 300 K for

50 ps using an isothermal-isobaric ensemble. Uniaxial tension along the x-axis is performed

at a constant engineering strain rate of 5×10^8 s^{-1} and temperature 300 K using Nosé–Hoover

thermostat[36,37]. At the same time, the stresses along y and z directions are controlled at zero

average value using Berendsen barostat[38]. During deformation, we compute the atomic

stress associated with each grain, and hence the stress-strain response of individual grains

is obtained.

2.2 Microstructure evolution during tension deformation

Figure 2.1b shows the system-level plastic flow stress σ as a function of twin

boundary spacing, where the stress is scaled by Young's modulus E. The top panel presents

the data for Al and Cu, and the bottom contains the results for Co, NiCoCr, and NiCoCrFeMn.

With decreasing the twin thickness from 3.75 to 0.63 nm, the second group of materials in

the bottom panel demonstrates a monotonic increase in flow stress. This continuous

strengthening is distinct from the strength softening, manifested in both Cu and Al at critical

spacing. Figure 2.1c summarizes all the data, plotting SFE against flow stress change $\Delta\sigma$

between the two smallest twin boundary spacings. The sign of $\Delta\sigma$ captures the strengthening

and softening effects, with a negative value indicating a decrease in strength. Interestingly,

the results suggest a possible correlation between SFT and TB strengthening effect in
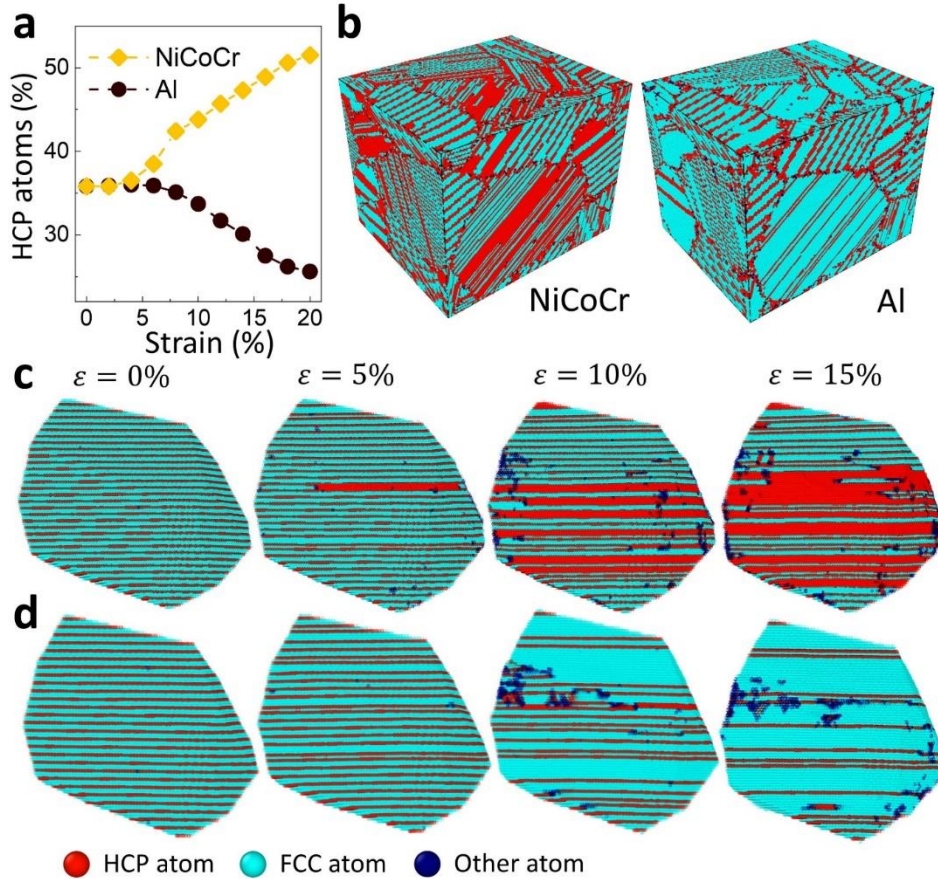
nanotwinned systems.

Figure 2.2 | Deformation structure evolutions in NiCoCr and Al. (a) The variation of hcp atom fraction as a function of tensile strain for NiCoCr and Al, as labeled. The corresponding structures at 15% strain are shown in **(b)**. Structure evolutions of an individual grain 5 in NiCoCr **(c)** and Al **(d)** at various strain stages. The red and light blue represent hcp and fcc, respectively. (red, light blue and dark blue represent HCP atom, FCC atom, and other atom respectively)

To reveal the mechanisms underlying the two types of behavior, we first present how the microstructure evolves during straining. Figure 2.2a shows the hcp-structured atom fraction as a function of tensile strain for two representative materials, NiCoCr (continuous strengthening) and Al (softening), for λ = 0.63 nm. The initial undeformed structure has ~35% hcp-structured atoms, and they are associated with the built TBs. Right after plastic yielding (~4% strain), the hcp fraction in NiCoCr rapidly increases, but it decreases in Al. At 20% strain, NiCoCr accumulates 50% hcp-structured atoms, and the hcp fraction in Al drops

to 25%. Looking at the deformed structures (Figure 2.2b), hcp thick layers are formed inside the NiCoCr grains. However, in Al, the initial TBs have been annihilated, suggesting drastically different dislocation and deformation mechanisms. In Figure 2.2c-d, we demonstrate the detailed structure evolution for an individual grain, deformed from 0% to 15%. It is evident that the nucleation and thickening of hcp phase (more than three hcp layers) in NiCoCr, resulted from partial dislocation glide on every other (111) plane. As the strain increases, consecutive partial motion and coalesce of hcp lamellae generate a large volume fraction of hcp phase. TB migration in Al, resulting from partial glide on neighboring planes, causes TBs interaction and annihilation. Because the two grains in Al and NiCoCr have the same orientation, it is intriguing that dislocation slip is considerably impacted by the SFE, which can bring about detwinning and hcp formation (martensite transformation).
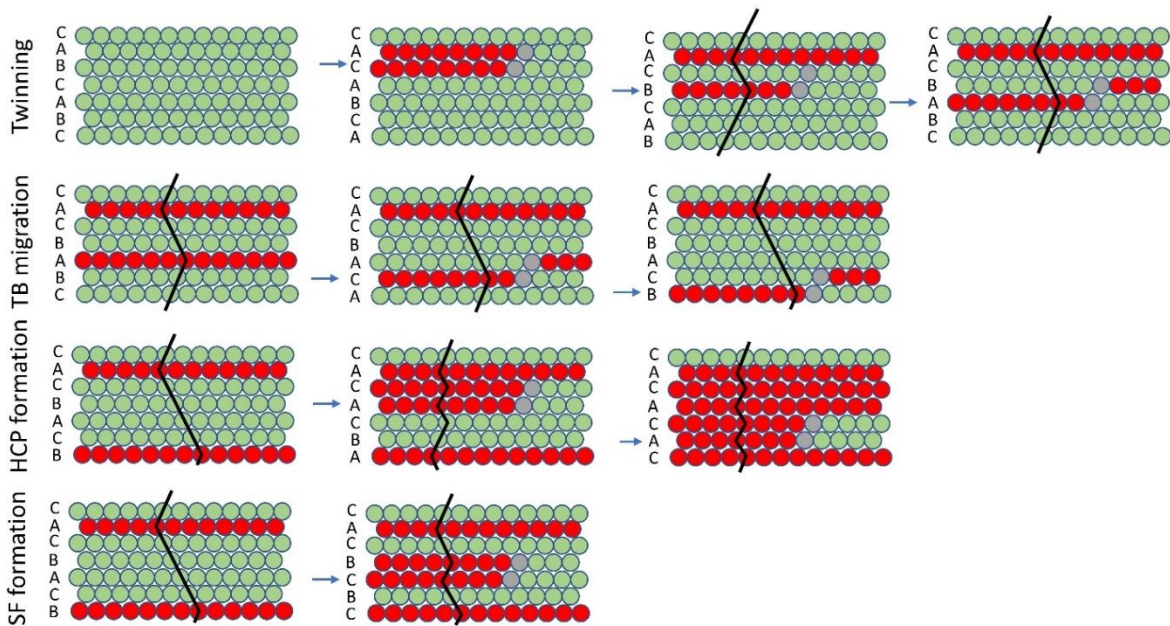

Figure 2.3| Typical formats that a partial dislocation modifies the FCC structure.

Depending on the grain orientation and Schmid's factors, dislocation slip in nanotwinned metals has three modes[39] (see Figure 1.1b), slip transfer mode (both slip plane

and Burgers vector inclined to TB), confined layer mode (slip plane is inclined to TB but Burgers vector parallel to TB), and parallel slip mode (both slip plane and Burgers vector parallel to TB, the soft mode). Next, we examine the dislocation slip mode, deformed structure, and local strain in NiCoCr and Al, aiming to understand the origin of continued strengthening.

2.3 Strengthening mechanisms
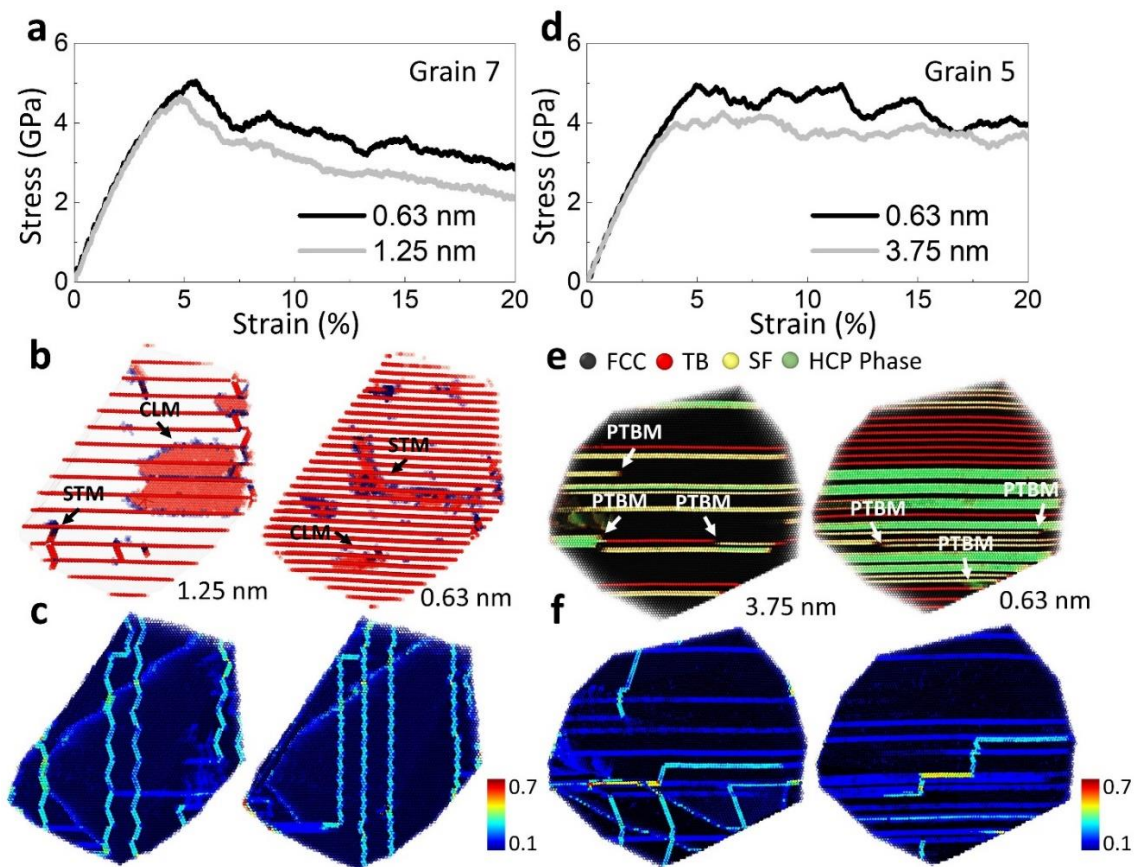
Figure 2.4 | Strengthening mechanisms in NiCoCr. (a) Strain-stress curves of grain 7 with twin thickness, 1.25 nm and 0.63 nm. **(b)** The corresponding deformation structures show the hard dislocation slip modes occur in both cases. **(c)** The atomic shear strain map indicates the slip traces from the hard modes. **(d-f)** shows the same data analysis for grain 5, which carries the soft dislocation mode. The red, yellow, and green colors represent fcc, TB, SF, and hcp lamella, respectively.

Figure 2.4 a-b shows the stress-strain curves for grain 7 and grain 5 of NiCoCr, both of which exhibit flow stress increase (strengthening) with decreasing the twin boundary spacing. Concerning grain 7, the deformed structure (Figure 3b) and plastic strain (Figure 2.4c) indicate that the two hard modes (slip transfer and confined layer) occurring in large boundary spacing (λ=1.25 nm) persist in small spacing as well (λ=0.63 nm). This suggests the TB strengthening mechanisms associated with two hard modes persevere with reducing λ. Grain 5 has the parallel slip mode predominating over the deformation. The left and right panels of Figure 2.4e show the deformed grain structures with initial λ spacing, 3.75 nm and 0.63 nm, respectively. While the same predominant parallel mode takes place in the grains, the resulting deformation structures manifest evident differences. For large twin thicknesses, partial dislocation slip causes TB migration, stacking fault formation, and hcp nucleation, depending on the relative location of partial slip to existing TBs. In contrast, the grain with a small twin thickness (0.63 nm) displays hcp lamellae, predominating over the deformation structure. Dislocation motion in densely packed TBs and strain-induced hcp phase can be the underpinning mechanisms behind the enhanced flow stress in grain 5.

2.4 Softening mechanisms

Unlike NiCoCr, the Al experiences strength softening by reducing the twin boundary spacing to 0.63 nm (Figure 2.1b), also reflected by the stress-strain curves of individual grains 7 and 5 (Figure 2.5a-b). Characterizing the dislocation modes and local plastic strain, we show the underlying softening mechanisms in these grains. Figure 2.5b shows the dislocation modes inside grain 7. For the twin thickness of 1.25 nm, the dislocation motion proceeds primarily through hard modes. However, for a smaller spacing of 0.63 nm (the same grain orientation), the soft mode involving partial slip parallel to the twin boundary

13

becomes more active. As for grain 5, the defect structure and local strain map (Figure 2.5e-f) indicate only partial dislocation is prevalent, and its motion causes the annihilation of TBs (detwinning). This observation implies the existence of a driving force that tends to remove the TBs from the nanotwinned structure, rooting from the high SFE.
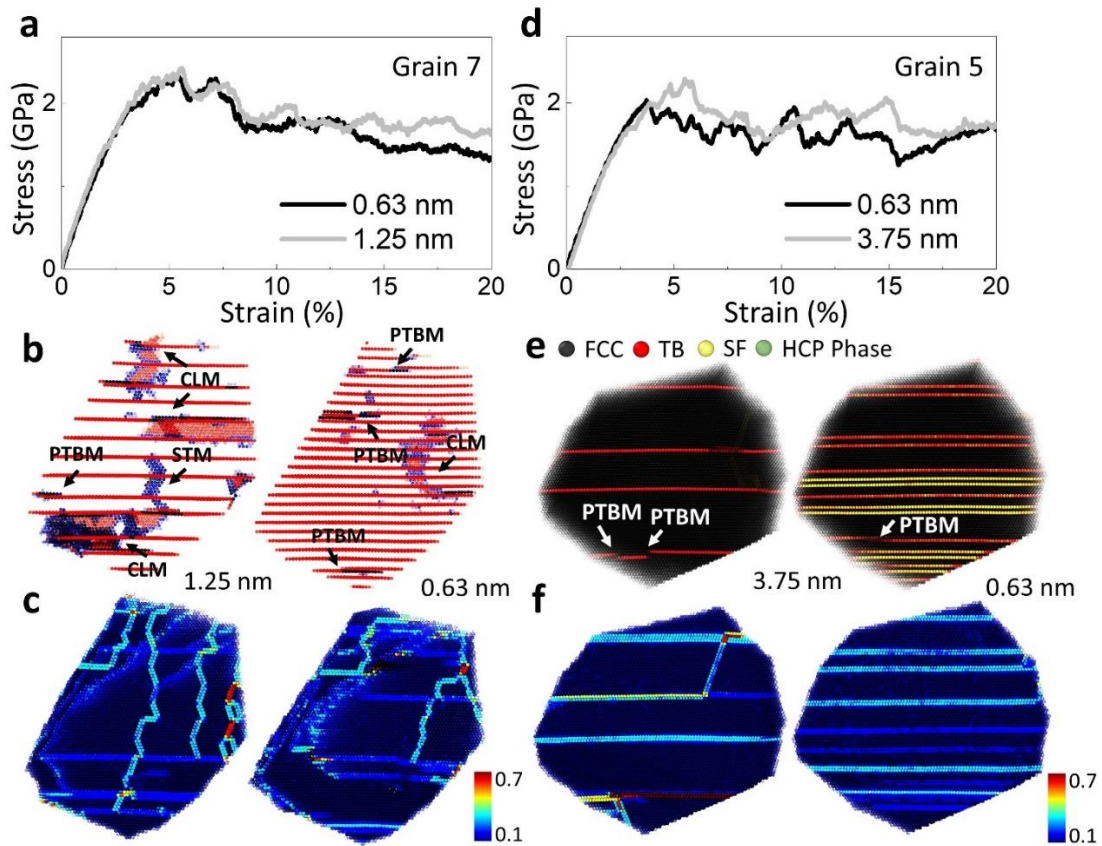
Figure 2.5 | Softening mechanisms in Al. (a) Strain-stress curves of grain 7 with twin thickness, 1.25 nm and 0.63 nm. **(b)** The corresponding deformation structures show the hard dislocation slip modes occur in twin thicknesses 1.25 nm. The soft mode is prevalent in twin thicknesses 0.63 nm. **(c)** The atomic shear strain map indicates the slip traces. **(d-f)** shows the same data analysis for grain 5. The soft dislocation mode causes TB annihilation and detwinning. The red and yellow colors represent fcc and SF, respectively.

Chapter 3 Brittle to Ductile Transition in Ta Metallic Glass

In this chapter, the role of structural heterogeneity, namely short- to medium-range order, in the deformability of monoatomic Ta metallic glass will be discussed.

3.1 Simulation model and methods

Uniaxial tension deformation. We used the embedded atom method (EAM)[40]potential, previously developed to model amorphous Ta, for describing the interatomic interactions. The initial bulk glass was simulated by quenching an equilibrated high-temperature liquid from 4,000 K down to 1 K at a finite cooling rate of 0.25 K/ps. The as-quenched glassy block was then tailored into cylindrical nanowires, 20 nm in diameter and 40 nm in length, containing approximately 6.56×10^5 Ta atoms. Starting from this prepared nanopillar, two independent simulations for aging and rejuvenation were instigated to prepare aged and rejuvenated nanowires, respectively. Specifically, the nanowire was relaxed at a temperature of 1,600 K (well below glass transition temperature of ~1,700 K), followed by slow cooling to 300 K, to generate the aged nanowire. The rejuvenated nanowire was acquired by heating the nanowire to 2,500 K for 50 ps, followed by fast quenching to 300 K. Both nanowires are fully relaxed at 300 K before uniaxial tension straining deformation at an engineering strain rate of 5×10^8 s^{-1}.

Local ICO density and its strain evolution. The slabs (20 nm × 40 nm × 6 nm) containing regions of the shear band and necking zone were extracted from the aged and rejuvenated nanowires, respectively, to construct the relationship between structure and deformation mode. To create the density map, we used a 2D Gaussian function to represent each icosahedron (ICO), defined as $\emptyset\left(x, y, X_i, Y_i, \omega_x, \omega_y\right) = \frac{1}{2\pi\omega_x\omega_y} \exp\left(-\frac{(x-X_i)^2}{2\omega_x^2} - \frac{(y-Y_i)^2}{2\omega_y^2}\right)$,
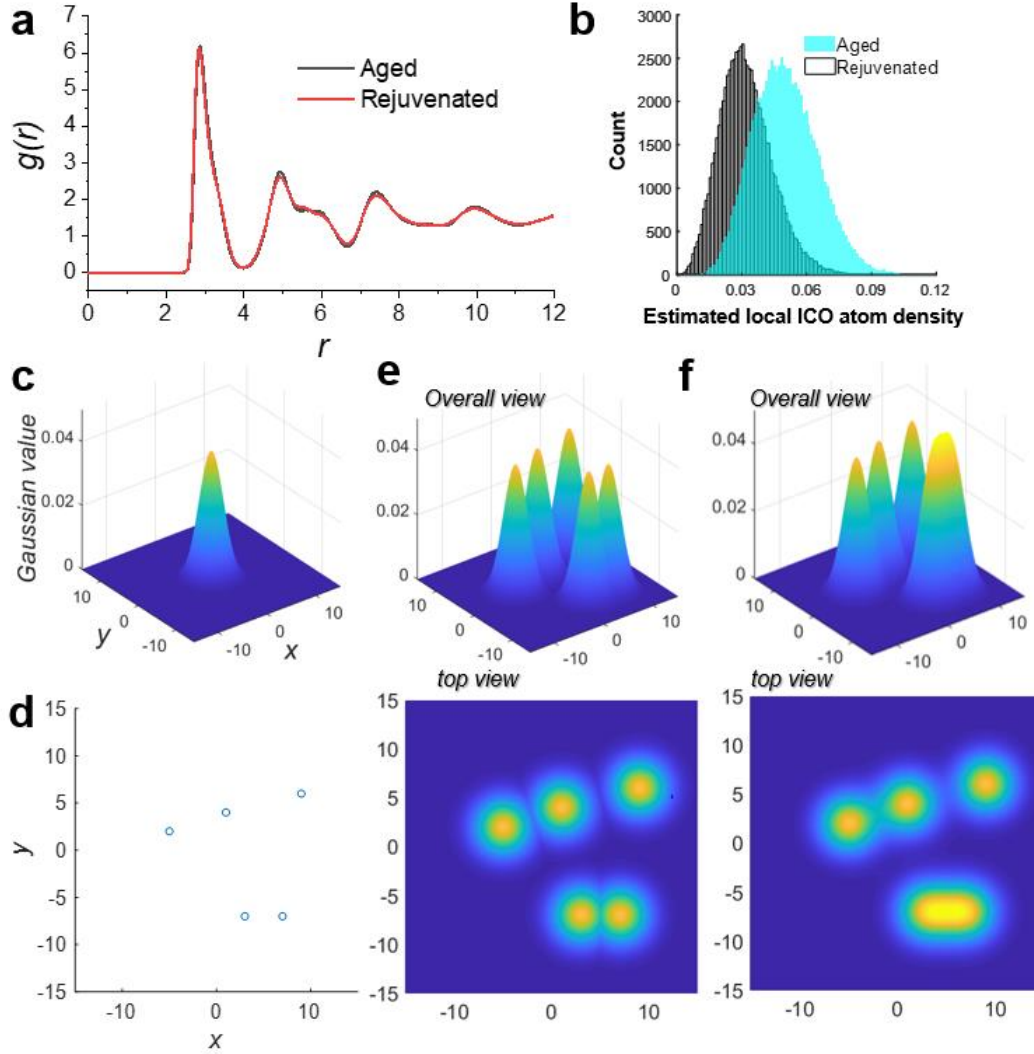
Figure 3.1 | Estimation method of the distribution of local ICO atom density. (a) Radial distribution functions for aged and rejuvenated nanowires. **(b)** Histograms of the local ICO atom density for aged and rejuvenated nanowires at 0% strain. **(c)** 2D Gaussian function used in this estimate. **(d)** A system containing 5 ICO atoms. **(e)** ICO atoms represented by a 2D Gaussian function. **(f)** Estimated distribution of the local ICO atom density.

where (X_i, Y_i) is the i-th ICO atom coordinate, and $\omega_x = \omega_y$ are the Gaussian width in the x- and y-directions, respectively. The distribution of the local ICO density was estimated by

$f(x, y) = \sum_{i=1}^{n} \varnothing\left(x, y, X_i, Y_i, \omega_x, \omega_y\right)$, where i ranges from 1 to n, and n is the total number of

ICOs in the system. Based on the radial distribution functions (Figure 3.1a), $\omega_x = \omega_y = 2$

was chosen to accurately capture each ICO atom and represent the local environment (see

Figure 3.1c). To construct a continuous density map, a mesh grid with a unit size of 1×1 Å^2 was established across the sample, with the density value $f(x, y)$ at each unit grid center (x, y) calculated and averaged over the slab thickness (6 nm). An example of the system containing 5 ICOs is presented in Figure 3.1d to f. To demonstrate the evolution of local ICO density from the initial state in the figure, a fixed color bar range is used for each nanowire at different strain states. The histograms of local ICO density for two nanowires at 0% strain are shown in Figure 3.1b, with the complete density evolution with respect to strain shown, for example, in Figure 3.6.
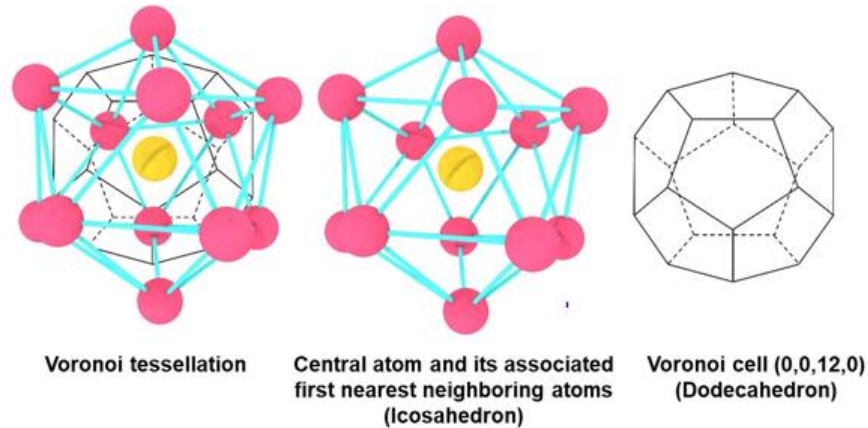

Voronoi tessellation   Central atom and its associated first nearest neighboring atoms (Icosahedron)   Voronoi cell (0,0,12,0) (Dodecahedron)

Figure 3.2 | Example of Voronoi tessellation. Illustrating how Voronoi tessellation is performed on a central atom (yellow) and associated first nearest neighboring atoms (red) and the corresponding Voronoi cell (black).

Short range order. Short-range order (SRO), the smallest ordering unit in metallic glasses (MGs), involves one central atom and its first nearest neighboring atoms. Voronoi tessellation is performed to characterize the geometrical qualities of SRO (Figure 3.2), where a polygon is established by bisecting each line connecting the central atom and one first nearest neighboring atom, and the polyhedron enclosed by the polygons between the central atom and its first neighboring atoms is called as a Voronoi cell. For a given atom, its

associated Voronoi cell can be denoted by the Voronoi index ($n3, n4, n5, …, ni$), where ni represents the number of i-edged polygons in a polyhedron. As such, the volume of the Voronoi cell to the central atom can be calculated as the atomic volume.

Medium range order. In this work, medium-range order (MRO) is considered in terms of the connectivity of atoms with the Voronoi index (0,0,12,0), which are also known as ICOs[414243] (Figure 3.3a). Given two ICO atoms and their associated first nearest-neighbor atoms, there are four types of possible connections in 3D space: vertex-sharing, edge-sharing, face-sharing, and volume-sharing[444529] (Figure 3.3b). Among all possible connections, only volume sharing has direct bonding between the two ICO atoms, where the two ICO atoms sit at the vertices of each other's Voronoi cell. In this case, they also have the largest shared volume, and hence the densest packing. Considering one central ICO atom and its Voronoi cell, if all the atoms at the vertices of the Voronoi cell are also ICO atoms, a small icosahedral crystalline pattern can be formed, and with the growth of such a unit, long-range order of icosahedra can be thus established. As a result, ICO atom networks connected by volume sharing are truly the intermediate condition that serves to bridge short-range order to long-range crystalline order. Thus, we can consider this as an indicator for probing the medium-range order in aged and rejuvenated nanowires. Figure 3.3c shows one such example of an ICO network with five atoms connected by volume sharing; the other ICO atoms that are not connected by volume sharing are considered as isolated ICO atoms.
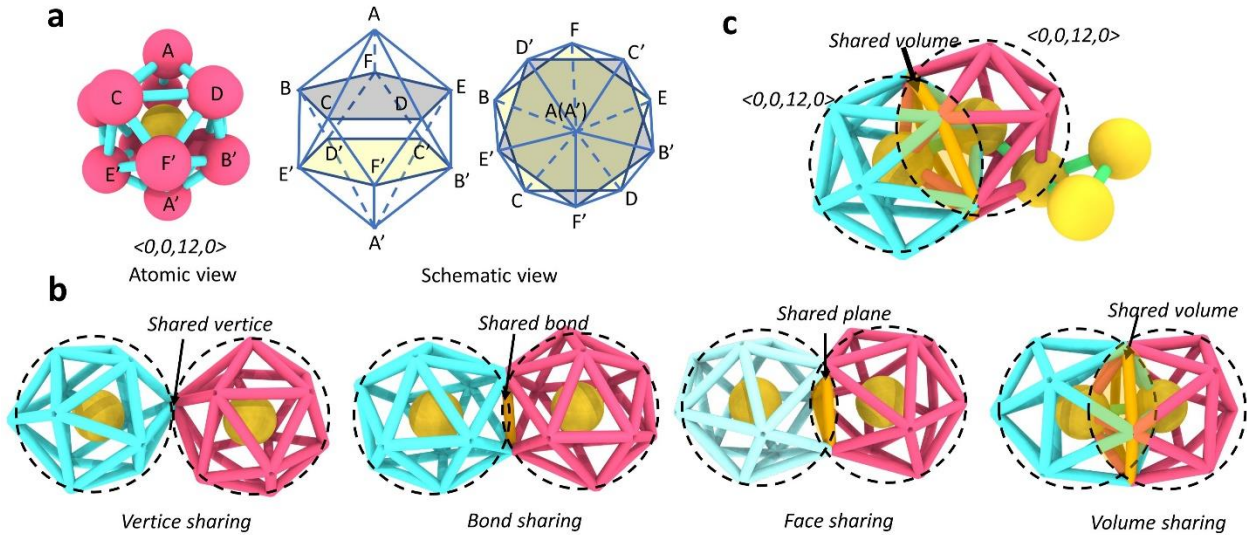
Figure 3.3 | Connectivity of icosahedron (ICO) atoms. (a) One ICO atom (yellow) and its associated first nearest neighbor atoms (pink) shown as atomic view and schematic view. **(b)** Four types of possible connections for two ICO atoms and their associated first nearest neighbor atoms (showing only the bonds). Dashed circles denote two individual ICO atoms and their associated first nearest neighbor atoms. **(c)** A 5-atom ICO network connected by volume sharing. Only the two first nearest neighboring shells (blue and pink) of ICO atoms (yellow) are shown. The green bonds denote the direct connection between ICO atoms. Each ICO atom sits at the first nearest neighboring shell of other ICO atoms.

3.2 Ductile and brittle fracture and its transition

Large-scale atomistic simulations were performed to explore the critical role of structural heterogeneity on the deformation of the Ta MG nanowires. Two samples with the same size but markedly different processing histories, including aging that creates a highly-relaxed state, and rejuvenation that generates an ultra-fast quenched state, were prepared for mechanical testing. In the aged nanowire (Figure 3.4a), the simulations show that local shear transformation events (STZs) were activated upon deformation, which accumulated gradually to form an incipient shear band at 16% strain. At the strain of 30%, a mature shear band was developed through increasing activation and percolation of the shear transformation events. In contrast, the triggered STZs in the rejuvenated nanowire spread

19

uniformly at a strain level below 30%, which gave rise to enhanced ductility accompanied by delayed necking localization at 50% strain (Figure 3.4b). The spatial and temporal evolutions of local plastic strain demonstrate a clear brittle-to-ductile transition from the
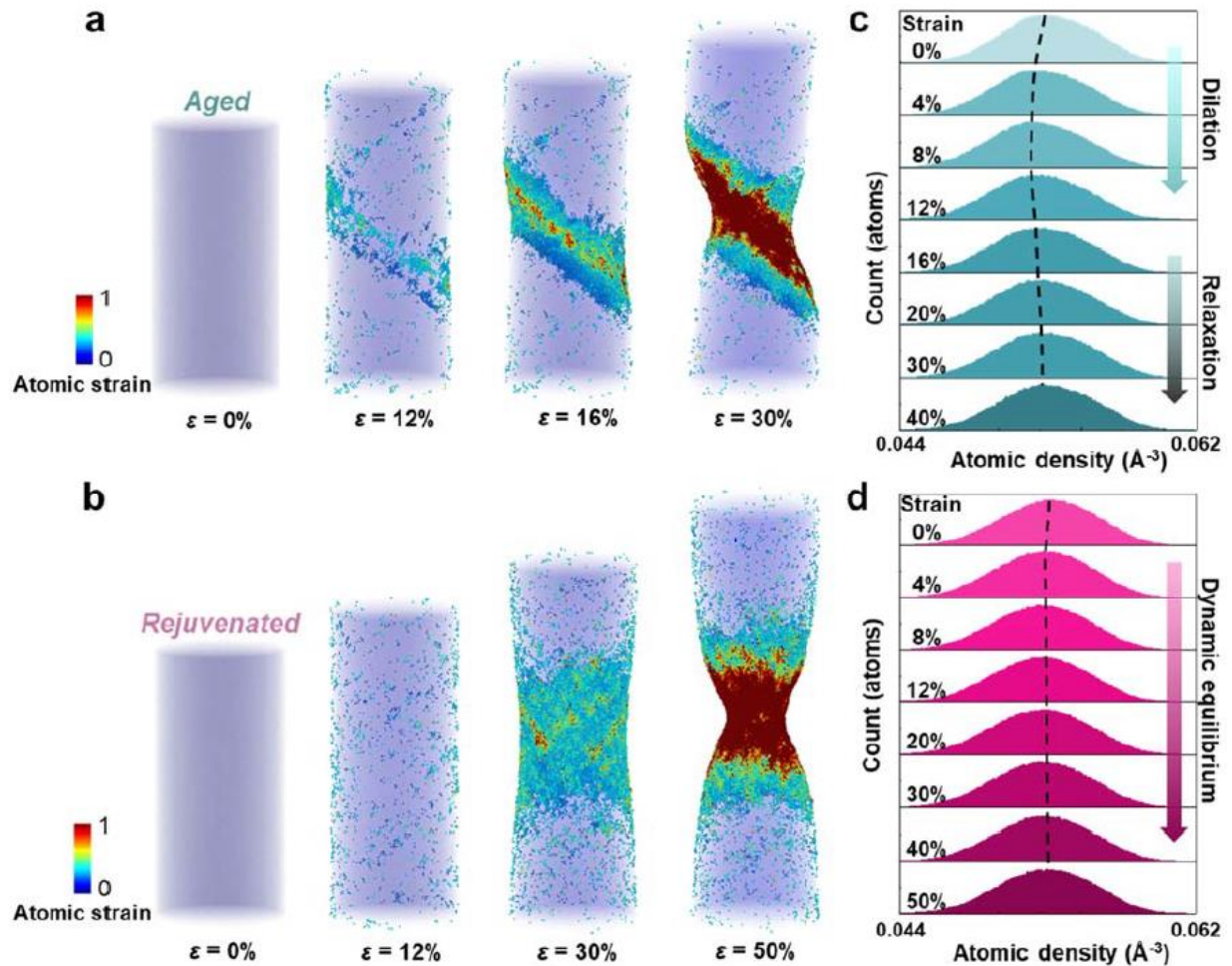

Figure 3.4 | Deformation behavior in aged and rejuvenated Ta MG nanowires. The structure evolutions of **(a)** aged and **(b)** rejuvenated nanowires with straining, respectively. The atoms are color-coded by atomic strain, and only the atoms with atomic shear strain higher than 0.3 are shown. The evolution of local atomic density distribution with the straining in **(c)** aged and **(d)** rejuvenated nanowires, respectively. The dashed black lines indicate the peak position of the distribution.

aged nanowire (shear banding) to the rejuvenated one (necking-like flow). Figure 3.4c-d

provides further quantification of the dynamic variations in the distribution of the atomic

density, i.e., the inverse of the atomic volume enclosed by the Voronoi cell of the central atom.

In the aged nanowire, the peak position of the atomic density gradually shifted to a smaller value before 12% strain (Figure 3.4c), implying the occurrence of stress-induced dilation and free volume accumulation during elastic deformation. Immediately after the yielding, at the formation of an incipient shear band at 16% strain, the decreasing trend in the peak in atomic density appeared to reverse with further increase in strain up to 40% strain, indicating that the applied strain has been accommodated in the shear band to enable the relaxation of the elastically deformed matrix. In contrast, for the rejuvenated nanowire, the peak in atomic density displayed no such variation with strain (Figure 3.4d), suggesting the existence of a relaxation process that can densify the structure and compensate for any dilation. This implies a strong correlation between local atomic structure and the overall deformation behavior of MGs. Additionally, both nanowires possess a similar average atomic volume of 18.90 ± 0.01 Å^3. Given the completely different deformation modes in these two types of nanowires, it is reasonable to speculate that the system-averaged atomic free volume should not be considered as the determining microstructural feature controlling the mechanical response of MGs.

3.3 Short-range order and its effect on the deformation mechanism

To elucidate the physical origin of brittle-to-ductile transition in the Ta MG nanowires with the same average atomic volume, we first analyze the evolution of atomic structure based on the short-range order. The SRO is characterized in terms of Voronoi polyhedra (see Figure 3.2), which represent the elemental building units that comprise the amorphous structure(15). Figure 3.5a presents and compares the statistical distributions of Voronoi polyhedra in the undeformed MG nanowires. The aged nanowire has an exponential-like
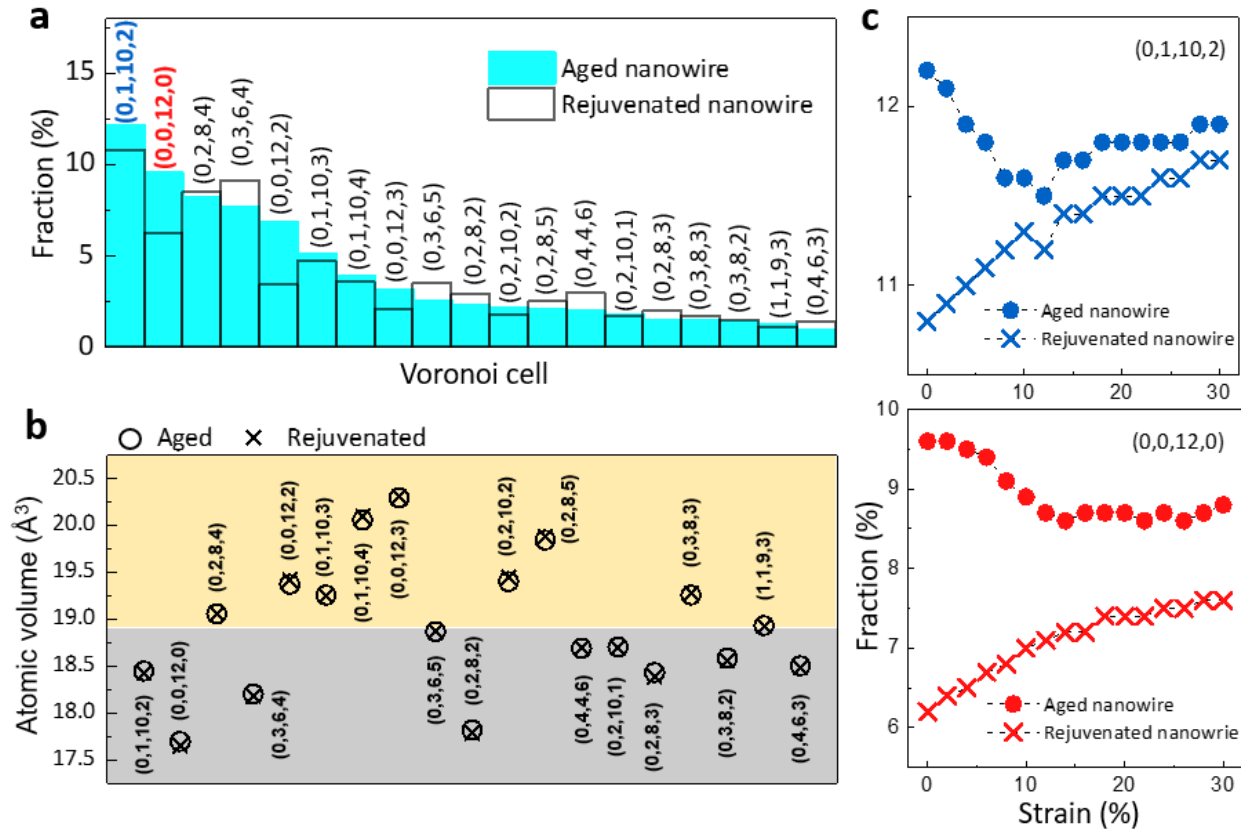
Figure 3.5 | Short-range order in aged and rejuvenated Ta MG nanowires. (a) Distributions of Voronoi polyhedra with a fraction greater than 1% in aged and rejuvenated nanowires, respectively. **(b)** Mean atomic volumes of Voronoi cells in aged and rejuvenated nanowires. The orange regime includes polyhedrons with atomic volume greater than average, and the grey regime includes polyhedra with an atomic volume that is smaller than the average. **(c)** Evolution of the fraction of (0,1,10,2) distorted icosahedra (blue) and (0,0,12,0) perfect icosahedra (red) as a function of applied strain in aged (solid circles) and rejuvenated (crosses) nanowires.

distribution with high concentrations of certain groups of polyhedra; in contrast, the rejuvenated nanowire exhibits a relatively-random distribution, suggestive of a thermal-induced propensity for structural homogeneity. In particular, the dense icosahedron (ICO) (0,0,12,0) and icosahedral-like (0,1,10,2) atomic motifs, which are the two most energetically-favored local atomic configurations in the aged nanowire, are appreciably reduced after rejuvenation; indeed, they are not the most preferred form of SRO in the rejuvenated nanowire. Given that the mean atomic volumes associated with polyhedral and
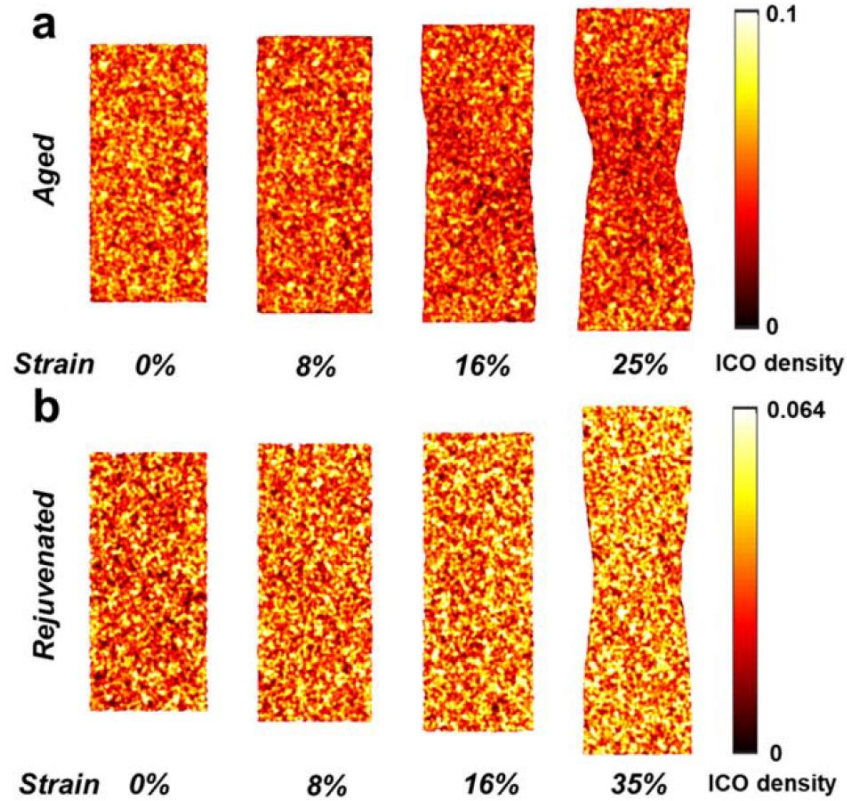
22

Figure 3.6 | The spatial distribution of ICO atoms kernel density. The evolution with strain **(a)** in the aged nanowire at 0% (initial), 8% (elastic regime), 16% (formation of shear banding), and 25% (further shear of shear banding) strain, and **(b)** in the rejuvenated nanowire at 0% (initial), 8% (elastic regime), 16% (after yielding), and 35% (necking) strain.

their distribution is the same in these two samples (Figure 3.5b), the fluctuation in the proportion of specific polyhedra, as well as the dynamic transformation between different types of Voronoi cells during straining, should provide the root cause for the variation in atomic volume distribution in the respective systems plotted in Figure 3.4c-d. Figure 3.5c shows the fractions of energetically favorable icosahedral-like motifs, i.e., (0,1,10,2) and ICO (0,0,12,0), as a function of the applied strain. Strikingly, the aged and rejuvenated systems demonstrate distinct behaviors in the early stage of deformation: the former involves a decrease in the fraction of icosahedral-like packing, yet the latter exhibits an increase in this fraction. The strain-induced accumulation of energetically-preferred clusters in the rejuvenated nanowire indicates structural relaxation and the resultant formation of lower

23

energy clusters during mechanical loading. Figure 3.6a-b presents the spatial evolutions of ICO clusters (SRO) in response to the mechanical strain, aiming to connect them with the necking and shear band activities. In the aged system (Figure 3.6a), the density of ICOs is appreciably reduced in the shear band region, indicating the local plastic deformation associated with shear banding formation would destroy the ICO packing. Regarding the rejuvenated nanowire (Figure 3.6b), however, ICOs tend to nucleate throughout the whole system, suggesting a strain-mediated homogeneous relaxation.

3.4 Medium range order and its effect on the deformation mechanism

Next, we discuss how medium-range order evolves and contributes to the deformation of Ta MGs. In Figure 3.7a-b, we show the spatial evolution of ICO networks (MRO) which are comprised of volume-shared ICOs. It is noted that the ICO networks are drastically reduced with the formation of a shear band. We further analyzed the statistical distribution of isolated ICO and connected ICOs (Figure 3.8) in the aged and rejuvenated systems. Interestingly both nanowires show nearly the same amount of isolated ICOs (~1.9%), but the aged system possesses more ICO-connected clusters (network). During mechanical straining, the ICO networks can be seen to be shrinking in the aged system, yet they are growing in the rejuvenated system, although the number of isolated ICOs remains essentially unchanged. This signifies that the ICO networks (i.e., MROs) are primarily responsible for plastic deformation and the observed brittle-to-ductile transition; as such, we can conclude that they dictate the deformability and mechanical response of the MG nanowires.

24
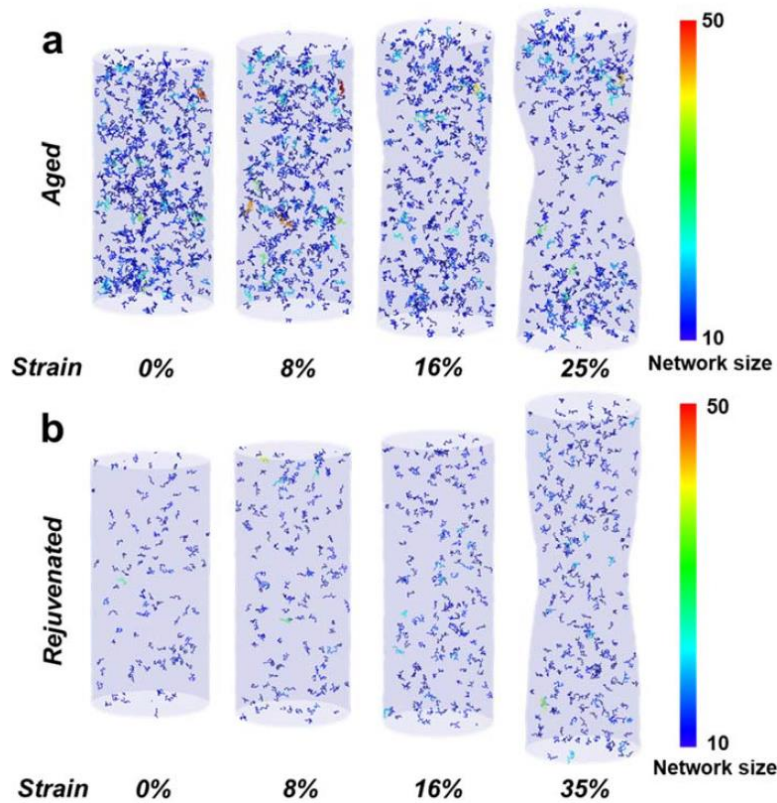
Figure 3.7 | The spatial distribution of ICO networks formed by volume sharing. The evolution with strain **(a)** in the aged nanowire at 0% (initial), 8% (elastic regime), 16% (formation of shear banding), and 20% (further shear of shear banding) strain, and **(b)** in the rejuvenated nanowire at 0% (initial), 8% (elastic regime), 16% (after yielding), and 35% (necking) applied strain.

Figure 3.8 | Atom fractions of isolated ICOs and ICO clusters. (a) Initial state. **(b)** After the shear band (25% strain) and necking (35% strain) formation.

25

Chapter 4 Summary and Conclusions

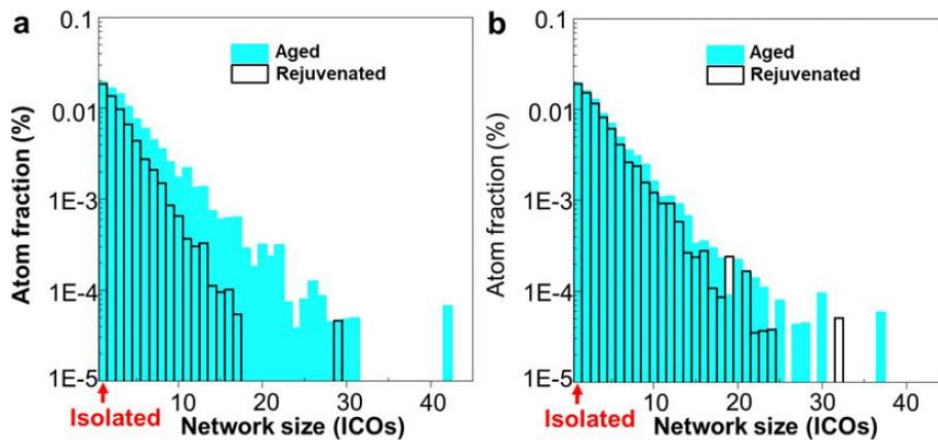This study manifests the effect of structural heterogeneity on the mechanical deformation behavior of metallic materials, and we demonstrate our understanding on nanotwinned metals and metallic glasses respectively:

Nanowtinned metals. Depending on the grain orientation, the introduced TBs to individual grains of polycrystal not only provide barriers to dislocation slip and also enables dislocation slip within TBs. With reducing the twin boundary spacing, the high SFE Al first experiences a strengthening effect followed by softening. This crossover is closely related to the dislocation mechanism change from hard mode to dislocation-nucleation-controlled soft mode[2]. Notably, we found that the dislocation slip (soft mode) results in TB migration and annihilation in nanotwinned Al, originating from its high SFE and inclination to remove TB and SF. However, for materials with low SFE, the soft dislocation mode gives rise to hcp lamella formation and growth. More importantly, the hard dislocation modes, which occur at large twin boundary spacing, also prevail in reduced spacing (even at 0.63 nm). The consistency of the dislocation mechanisms and its insensitivity to twin thickness are manifested as continued strengthening in nanotwinned NiCoCr.

Our results reveal that the strongest twin size (twin boundary spacing) and the dislocation deformation modes vary in materials with different SFEs. The vast compositional space of MPEAs and their broadly tunable SFE provide an exciting avenue for manipulating dislocation mechanisms and the ultimate strength of nanotwinned-MPEAs. An additional aspect of our study is a suggestion to explore the theoretical studies, which have well

addressed the scaling law[46] and break-down[47,48] of the Hall–Petch effect in polycrystalline metals.

Monoatomic Ta MGs. We reveal in this study the origin of the brittle-to-ductile transition in monatomic Ta MGs, by tailoring the intrinsic structural heterogeneity via varying thermal treatment and tracking their dynamic evolution upon deformation. Structural heterogeneity is found to be an intrinsic factor in controlling the deformation modes of monoatomic MG nanowires, in contrast to the widely accepted averaged structural state criterion[8]. The results demonstrate that the origin of the brittle-to-ductile transition in Ta MG nanowires is more associated with the structural features of medium-range order rather than with short-range order. These findings establish critical correlations between the inherent structure of metallic glasses and their deformation modes, which we believe advances the current understanding of structure-property relations in a broad class of MG materials. Further, this study is of technological importance for the future design of MGs with controllable mechanical properties.

Reference

1.   Wu, X. & Zhu, Y. Heterogeneous materials: a new class of materials with unprecedented mechanical properties. *Mater. Res. Lett.* **5**, 527–532 (2017).

2.   Li, X., Wei, Y., Lu, L., Lu, K. & Gao, H. Dislocation nucleation governed softening and maximum strength in nanotwinned metals. *Nature* **464**, 877–880 (2010).

3.   Ke, L. Making strong nanomaterials ductile with gradients. *Science (80-.).* **345**, 1455 LP – 1456 (2014).

4.   Han Wang and Penghui Cao. Strength softening mitigation in bimodal structured metals. *J. Appl. Phys.* **045102**, (2022).

5.   Sun, J. *et al.* A novel process to obtain lamella structured low-carbon steel with bimodal grain size distribution for potentially improving mechanical property. *Mater. Sci. Eng. A* **785**, 139339 (2020).

6.   Greer, A. L., Cheng, Y. Q. & Ma, E. Shear bands in metallic glasses. *Mater. Sci. Eng. R Reports* **74**, 71–132 (2013).

7.   Hufnagel, T. C., Schuh, C. A. & Falk, M. L. Deformation of metallic glasses: Recent developments in theory, simulations, and experiments. *Acta Mater.* **109**, 375–393 (2016).

8.   Sun, Y., Concustell, A. & Greer, A. L. Thermomechanical processing of metallic glasses: Extending the range of the glassy state. *Nat. Rev. Mater.* **1**, (2016).

9.   Jiang, F. *et al.* Shear transformation zone volume determining ductile-brittle transition of bulk metallic glasses. *Acta Mater.* **59**, 2057–2068 (2011).

10.   Pan, J. *et al.* Extreme rejuvenation and softening in a bulk metallic glass. *Nat. Commun.* **9**, (2018).

11.   Jang, D. & Greer, J. R. Transition from a strong-yet-brittle to astronger-and-ductile state by size reductionofmetallicglasses. *Nat. Mater.* **9**, 215–219 (2010).

12.   Magagnosc, D. J. *et al.* Effect of ion irradiation on tensile ductility, strength and fictive temperature in metallic glass nanowires. *Acta Mater.* **74**, 165–182 (2014).

13.   Zhu, T. & Li, J. Ultra-strength materials. *Prog. Mater. Sci.* **55**, 710–757 (2010).

14.   Ma, E. & Zhu, T. Towards strength–ductility synergy through the design of heterogeneous nanostructures in metals. *Mater. Today* **20**, 323–331 (2017).

15.   Sun, L., He, X. & Lu, J. Nanotwinned and hierarchical nanotwinned metals: A review of experimental, computational and theoretical efforts. *npj Comput. Mater.* **4**, 1–18 (2018).

16.   Jin, Z. H. *et al.* The interaction mechanism of screw dislocations with coherent twin boundaries in different face-centred cubic metals. *Scr. Mater.* **54**, 1163–1168 (2006).

17. Jin, Z. H. *et al.* Interactions between non-screw lattice dislocations and coherent twin boundaries in face-centered cubic metals. *Acta Mater.* **56**, 1126–1135 (2008).

18. Wei, Y. Scaling of maximum strength with grain size in nanotwinned fcc metals. *Phys. Rev. B* **83**, 132104 (2011).

19. Xiao, J. & Deng, C. Continuous strengthening in nanotwinned high-entropy alloys enabled by martensite transformation. *Phys. Rev. Mater.* **4**, 043602 (2020).

20. Li, Z., Pradeep, K. G., Deng, Y., Raabe, D. & Tasan, C. C. Metastable high-entropy dual-phase alloys overcome the strength-ductility trade-off. *Nature* **534**, 227–230 (2016).

21. Ding, J., Yu, Q., Asta, M. & Ritchie, R. O. Tunable stacking fault energies by tailoring local chemical order in CrCoNi medium-entropy alloys. *Proc. Natl. Acad. Sci. U. S. A.* **115**, 8919–8924 (2018).

22. Wei, S. & Tasan, C. C. Deformation faulting in a metastable CoCrNiW complex concentrated alloy: A case of negative intrinsic stacking fault energy? *Acta Mater.* **200**, 992–1007 (2020).

23. Guo, H. *et al.* Tensile ductility and necking of metallic glass. *Nat. Mater.* **6**, 735–739 (2007).

24. Yi, J., Wang, W. H. & Lewandowski, J. J. Sample size and preparation effects on the tensile ductility of Pd-based metallic glass nanowires. *Acta Mater.* **87**, 1–7 (2015).

25. Cockayne, D. J. H. The study of nanovolumes of amorphous materials using electron scattering. *Annu. Rev. Mater. Res.* **37**, 159–187 (2007).

26. Sheng, H. W. *et al.* Polyamorphism in a metallic glass. *Nat. Mater.* **6**, 192–197 (2007).

27. Ma, D., Stoica, A. D. & Wang, X. L. Power-law scaling and fractal nature of medium-range order in metallic glasses. *Nat. Mater.* **8**, 30–34 (2009).

28. Pan, J., Ivanov, Y. P., Zhou, W. H., Li, Y. & Greer, A. L. Strain-hardening and suppression of shear-banding in rejuvenated bulk metallic glass. *Nature* **578**, 559–562 (2020).

29. Sheng, H. W., Luo, W. K., Alamgir, F. M., Bai, J. M. & Ma, E. Atomic packing and short-to-medium-range order in metallic glasses. *Nature* **439**, 419–425 (2006).

30. Cheng, Y. Q. & Ma, E. Atomic-level structure and structure-property relationship in metallic glasses. *Prog. Mater. Sci.* **56**, 379–473 (2011).

31. Sheng, H. W., Kramer, M. J., Cadien, A., Fujita, T. & Chen, M. W. Highly optimized embedded-atom-method potentials for fourteen FCC metals. *Phys. Rev. B - Condens. Matter Mater. Phys.* **83**, 1–20 (2011).

32. Liu, X. Y., Ercolessi, F. & Adams, J. B. Aluminium interatomic potential from density functional theory calculations with improved stacking fault energy. *Model. Simul. Mater. Sci. Eng.* **12**, 665–670 (2004).

33. Foiles, S. M., Baskes, M. I. & Daw, M. S. Embedded-atom-method functions for the fcc

metals Cu, Ag, Au, Ni, Pd, Pt, and their alloys. *Phys. Rev. B* **33**, 7983–7991 (1986).

34. Pun, G. P. P. & Mishin, Y. Embedded-atom potential for hcp and fcc cobalt. *Phys. Rev. B - Condens. Matter Mater. Phys.* **86**, 1–9 (2012).

35. Choi, W. M., Jo, Y. H., Sohn, S. S., Lee, S. & Lee, B. J. Understanding the physical metallurgy of the CoCrFeMnNi high-entropy alloy: An atomistic simulation study. *npj Comput. Mater.* **4**, 1–9 (2018).

36. Nosé, S. & Nosi~, S. Molecular Physics A molecular dynamics method for simulations in the canonical ensemble A molecular dynamics method for simulations in the canonical ensemblet. *Mol. Phys.* **52**, 255–268 (1984).

37. G.Hoover, W. Canonical dynamics: Equilibrium phase-space distributions. *Phys. Rev. A* **31**, (1985).

38. Berendsen, H. J. C., Postma, J. P. M., Van Gunsteren, W. F., Dinola, A. & Haak, J. R. Molecular dynamics with coupling to an external bath. *J. Chem. Phys.* **81**, 3684–3690 (1984).

39. Lu, K. Stabilizing nanostructures in metals using grain and twin boundary architectures. *Nat. Rev. Mater.* **1**, (2016).

40. Zhong, L., Wang, J., Sheng, H., Zhang, Z. & Mao, S. X. Formation of monatomic metallic glasses through ultrafast liquid quenching. *Nature* **512**, 177–180 (2014).

41. Hwang, J. *et al.* Nanoscale structure and structural relaxation in Zr 50Cu 45Al 5 bulk metallic glass. *Phys. Rev. Lett.* **108**, 1–5 (2012).

42. Wakeda, M. & Shibutani, Y. Icosahedral clustering with medium-range order and local elastic properties of amorphous metals. *Acta Mater.* **58**, 3963–3969 (2010).

43. Pekin, T. C. *et al.* Direct measurement of nanostructural change during in situ deformation of a bulk metallic glass. *Nat. Commun.* **10**, 1–7 (2019).

44. Luo, W. K., Sheng, H. W. & Ma, E. Pair correlation functions and structural building schemes in amorphous alloys. *Appl. Phys. Lett.* **89**, (2006).

45. Ding, J., Ma, E., Asta, M. & Ritchie, R. O. Second-nearest-neighbor correlations from connection of atomic packing motifs in metallic glasses and liquids. *Sci. Rep.* **5**, 1–9 (2015).

46. Di Leo, C. V. & Rimoli, J. J. New perspectives on the grain-size dependent yield strength of polycrystalline metals. *Scr. Mater.* **166**, 149–153 (2019).

47. Argon, A. S. & Yip, S. The strongest size. *Philos. Mag. Lett.* **86**, 713–720 (2006).

48. Xiao, J. & Deng, C. Ultimate Strength of Nanotwinned Face-Centered Cubic Metals. *Phys. Rev. Lett.* **125**, (2020).